Multifunctional Theranostic Agent of $Cu_2(OH)PO_4$ Quantum Dots for Photoacoustic Image-Guided Photothermal/Photodynamic Combination Cancer Therapy

Wei Guo,[†,‡] Zhenyu Qiu,[‡] Chongshen Guo,*[,†,‡] Dandan Ding,[‡] Tianchan Li,[†,‡] Fei Wang,[†] Jianzhe Sun,[‡] Nannan Zheng,[†,‡] and Shaoqin Liu*[,†,‡]

[†]School of Life and Technology and [‡]Key Laboratory of Microsystem and Microstructure (Ministry of Education), Harbin Institute of Technology, Harbin 150080, China

Ⓢ *Supporting Information*

ABSTRACT: Image-guided phototherapy is considered to be a prospective technique for cancer treatment because it can provide both oncotherapy and bioimaging, thus achieving an optimized therapeutic efficacy and higher treatment accuracy. Compared to complicated systems with multiple components, using a single material for this multifunctional purpose is preferable. In this work, we strategically fabricated poly(acrylic acid)- (PAA-) coated $Cu_2(OH)PO_4$ quantum dots [denoted as $Cu_2(OH)PO_4@PAA$ QDs], which exhibit a strong near-infrared photoabsorption ability. As a result, an excellent photothermal conversion ability and the photoactivated formation of reactive oxygen species could be realized upon NIR irradiation, concurrently meeting the basic requirements for photothermal and photodynamic therapies. Moreover, phototherapeutic investigations on both cervical cancer cells in vitro and solid tumors of an in vivo mice model illustrated the effective antitumor effects of $Cu_2(OH)PO_4@PAA$ upon 1064-nm laser irradiation, with no detectable lesions in major organs during treatment. Meanwhile, $Cu_2(OH)PO_4@PAA$ is also an exogenous contrast for photoacoustic tomography (PAT) imaging to depict tumors under NIR irradiation. In brief, the $Cu_2(OH)PO_4@PAA$ QDs prepared in this work are expected to serve as a multifunctional theranostic platform.

KEYWORDS: $Cu_2(OH)PO_4$, photothermal therapy, photodynamic therapy, theranostics, photoacoustic imaging
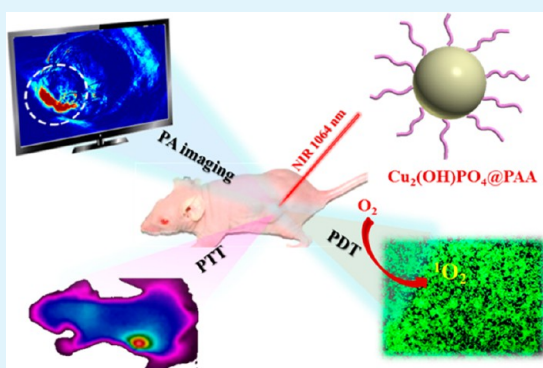
1. INTRODUCTION

Cancer is still among the major causes of fatality in humans today.[1−3] However, clinical therapies such as radiotherapy and chemotherapy often cause inevitable side effects to the immune system and healthy tissues, hence motivating scientists to seek some new therapeutic alternatives with minimal invasion and high spatial precision.[4−6] An important current research branch is phototherapy, particularly photothermal therapy (PTT) and photodynamic therapy (PDT). The implementation of PTT requires a near-infrared- (NIR-) absorbing nanomaterial to induce on-site hyperthermia for irreversible cellular damage or even death of tumor cells, whereas PDT requires a photo-sensitizer (PS) to generate reactive oxygen species (ROS) to eliminate cancer tissues.[7−18] Although both PTT and PDT have attracted much scientific attention, they also suffer from their own inherent drawbacks. For example, PDT efficacy deteriorates gradually with time of treatment as a result of the depletion of oxygen in the tissues.[19] For PTT, the major shortcoming is hyperthermia-induced heat shock, which can weaken the treatment efficacy by suppressing the apoptosis of malignant cells.[20] Therefore, some effort has been focused on the combination of PDT and PTT to engender a synergistic treatment outcome. Nonetheless, integrating photothermal nanomaterials with photosensitizers can lead to mutual interference, mismatch of the absorption edge, and a complex PDT/PTT system. As a consequence, use of a single material to realize the characteristics of both PDT and PTT will undoubtedly promote the overall phototherapeutic efficiency and make the PDT/PTT synergistic system easier to operate.

Recently, image-guided theranostic systems have emerged as an extremely important strategy for tumor therapy with high accuracy through visualization of the tumor site or tumor microenvironment during treatment.[21−29] Among various imaging modalities, photoacoustic tomography (PAT) imaging has attracted more attention because of its high spatial resolution, noninvasiveness, and deep penetration. The PAT modality is based on the detection of ultrasonic waves produced by a biological tissue or a PAT contrast agent when treated with laser pulses to induce transient thermoelastic expansion.[30−34] Hence, in essence, PAT also relies on an NIR-

activated photothermal conversion phenomenon induced by biological tissue or photothermal nanomaterials. In this regard, PAT is in accordance with PTT and is compatible with PDT/PTT combination therapy. For this reason, it might be possible to simultaneously produce local hyperthemia, ROS, and a photoacoustic signal upon single laser irradiation by selecting an applicable species, thus realizing PAT-guided photothermal/photodynamic combination cancer therapy.

$Cu_2(OH)PO_4$ seems like an ideal candidate for PAT image-guided phototherapy. $Cu_2(OH)PO_4$ exhibits strong optical absorbance in the NIR range of 800−1400 nm, where both an NIR-irradiation-induced hyperthemia effect and photoacoustic signal are highly expected. Moreover, $Cu_2(OH)PO_4$ was previously reported to be an NIR-activated photocatalyst, with the photosensitive formation of ROS by $Cu_2(OH)PO_4$ under NIR irradiation already confirmed.[35] Nevertheless, hardly any efforts have been directed toward the development of $Cu_2(OH)PO_4$ for biotherapy because of some distinct shortcomings such as difficulties in controlling morphology, reducing particle size, and achieving surface modification. Although PAT-imaging-guided PDT/PTT systems have been attempted with a "multiple-components-in-one" strategy by some research groups, the main drawbacks of these multifunctional systems include complicated chemical syntheses,[36,37] mutual interference,[38] and poor robustness.[39,40] In this work, we fabricated poly(acrylic acid)- (PAA-) coated $Cu_2(OH)PO_4$ quantum dots by a simple hydrothermal method and applied this material as a trifunctional theranostic agent that exhibited PAT-imaging-induced ability and PDT/PTT dual-therapeutic functions in the second biological windows for cancer therapy. Compared to common theranostic systems with multiple components, $Cu_2(OH)PO_4$@PAA is simple in composition and can avoid all of the above-mentioned shortcomings. In brief, this work proposes a "one-for-all" theranostic agent that is more promising than the common "all-in-one" theranostic systems.

2. EXPERIMENTAL SECTION

2.1. Materials. Unless specified otherwise, all chemicals were of analytical grade and were used without further purification. Copper nitrate trihydrate, sodium phosphate dibasic dodecahydrate, and *N,N*-dimethylformamide were obtained from Aladdin (Shanghai, China). Poly(acrylic acid) sodium salt (PAA, M_w = 1800), calcein AM, propidium iodide (PI), 3-[4,5-dimethylthialzol-2-yl]-2,5-diphenyltetrazolium bromide (MTT), 1,3-diphenylisobenzofuran (DPBF), and 2′,7′-dichlorodihydrofluorescein diacetate (H_2DCFDA) were obtained from Sigma-Aldrich. A reactive oxygen species assay kit was obtained from Shanghai Yi Sheng Biotechnology Co. Ltd.

2.2. Synthesis of $Cu_2(OH)PO_4$@PAA Quantum Dots. The $Cu_2(OH)PO_4$@PAA nanoparticles were prepared by a hydrothermal method. First, 0.29 g of $Cu(NO_3)_2$·$3H_2O$ and 0.35 g of PAA were dissolved in 30 mL of distilled water under magnetic stirring. Then, 30 mL (7.13 mg·mL^{-1}) of Na_2HPO_4·$12H_2O$ solution was added dropwise to the above light-blue mixed solution under constant stirring for 2 h. After that, the pH value of the resulting suspension was adjusted to 7. Thereafter, the mixed solution was transferred into a Teflon-lined autoclave with an internal volume of 100 mL, and the hydrothermal reaction was conducted in an electric oven at 120 °C for 6 h. After the reaction had completed, the light-green product was centrifuged and washed with water and ethanol. Finally, $Cu_2(OH)PO_4$@PAA was homogeneously dispersed in water by ultrasonic dispersion for 30 min.

2.3. Characterization. Transmission electron microscopy (TEM) images were obtained on a JEM-1400 microscope at an acceleration voltage of 100 kV. The phase nature of the sample was determined by X-ray diffraction (XRD, Shimadzu XD-D1). The optical properties were measured on a spectrophotometer (U-4100, Hitachi). Thermogravimetric analysis (TGA, Rigaku, TG8101D) was performed on samples from room temperature to 900 °C at a heating rate of 10 °C/min in the air. MTT [3-(4,5-dimethylthiazol-2-yl)-2,5-diphenyltetrazolium bromide] experiments were performed using a microplate reader (Infinite M200, Tecan).

2.4. Cell Culture. HeLa cells (cervical cancer cell line) were cultured in a monolayer in RPMI-1640 medium. Cells were supplemented with 10% (v/v) fetal bovine serum (FBS, Clark, Australia Origin) and penicillin/streptomycin (100 U mL^{-1} and 100 mg mL^{-1}, respectively, Gibco) in a humidified 5% CO_2 atmosphere at 37 °C.

2.5. Detection of ROS. The extracellular ROS generation of a sample was detected using DPBF as a probe.[41] Briefly, 20 μL of *N,N*-dimethylformamide solution containing DPBF (1 mg/mL) was added to a control group of 3 mL of pure water or 3 mL of $Cu_2(OH)PO_4$@PAA solution. After that, these two solutions were irradiated with a 1064-nm laser for various durations. After centrifugation, the optical absorbance of each solution at 410 nm was measured on a spectrophotometer. Then, the detection of the intracellular ROS level was performed on HeLa cell lines by staining with the H_2DCFDA probe.[42] For these experiments, 5×10^3 cells were seeded into a six-well plate and incubated at 37 °C in a humidified atmosphere with 5% CO_2 for 24 h. HeLa cells were next incubated with 200 μL of $Cu_2(OH)PO_4$@PAA (250 μg/mL) at 37 °C for 24 h. The positive control cells were treated with 200 μL of (50 mM) H_2O_2 at 37 °C for 30 min. Then, the cells were incubated with 50 μL of H_2DCFDA [10 mM in dimethyl sulfoxide (DMSO)] for another 1 h at 37 °C. After that, the cells were rinsed with PBS twice and irradiated under the 1064-nm laser (2 W/cm^2) for 5 min. Visualization of ROS was immediately measured with an Olympus BX53 fluorescence microscope using an excitation of 488 nm and an emission of 515−540 nm. Intracellular ROS generation was also analyzed using a flow cytometer with 2′,7′-dichlorodihydrofluorescein diacetate (H_2DCFDA) staining. Briefly, HeLa cells (2×10^5 cells/plate) were grown on six-well plates for 24 h. Then, the HeLa cells were divided into four groups: (1) control group without any treatment, (2) group treated with only light irradiation (1064-nm laser, 2 W/cm^2), (3) group treated with $Cu_2(OH)PO_4$@PAA QDs (250 μg/mL) only, and (4) group treated with NIR activation and $Cu_2(OH)PO_4$@PAA QDs. The $Cu_2(OH)PO_4$@PAA (250 μg/mL, 1 mL) was added to the samples of the corresponding groups and incubated with cells for 4 h. After the the four different groups of samples had been washed with phosphate-buffered saline (PBS), 10 μM of H_2DCFDA was added, and the samples were incubated for another 30 min. The samples of groups 2 and 4 were next exposed to NIR irradiation for 10 min. Finally, the washed cells were resuspended in PBS and measured using a flow cytometer (FCM, Becton Dickinson) with excitation set at 488 nm.

2.6. In Vitro and in Vivo PAT Imaging. In vitro and in vivo PAT imaging experiments were performed on a MSOT inVision 128 system. Briefly, 1 mL of $Cu_2(OH)PO_4$@PAA dispersion at different concentrations was added to the agar-phantom container and placed in the testing system for signal detection in vitro. The in vivo PAT imaging of $Cu_2(OH)PO_4$@PAA was carried out on HeLa tumor-bearing mice. The PAT imaging data of the tumor site were collected before and after intratumoral or intravenous injection of $Cu_2(OH)PO_4$@PAA solution (100 μL, 2 mg/mL).

2.7. Cytotoxity Assay. The viability of cells in the presence of $Cu_2(OH)PO_4$@PAA was investigated using a standard MTT assay. The assay was carried out in triplicate as follows: Cells were seeded into 96-well plates at a density of 1×10^4 per well in 200 μL of media and grown overnight. The cells were then incubated with a series of concentrations of $Cu_2(OH)PO_4$@PAA for 24 h. Following this incubation, the cells were incubated in medium containing 20 μL of 5 mg mL^{-1} MTT for 4 h. Then, the medium with MTT was removed, and 150 mL of DMSO was added to dissolve formazan crystals at room temperature for 30 min. Then, the absorbance was measured at 490 nm by multidetection microplate reader (Synergy HT, BioTek Instruments Inc., Winooski, VT). For in vitro PDT experiments, HeLa
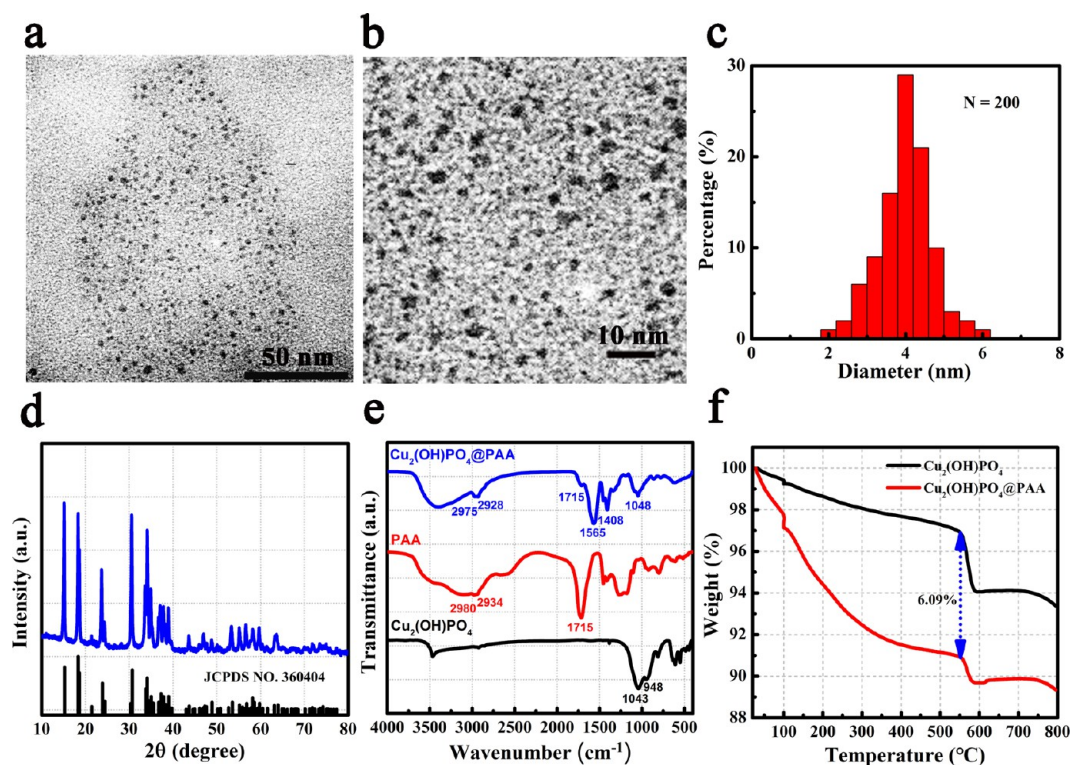
Figure 1. (a,b) TEM images, (c) particle size distribution, and (d) XRD pattern (JCPDS no. 360404 shown as a reference) of $Cu_2(OH)PO_4@PAA$. (e) FT-IR spectra of $Cu_2(OH)PO_4$, PAA, and $Cu_2(OH)PO_4@PAA$. (f) Thermogravimetric (TG) curves of $Cu_2(OH)PO_4$ and $Cu_2(OH)PO_4@PAA$.

cells seeded in 96-well plates were incubated with $Cu_2(OH)PO_4@$ PAA (250 μg/mL) for 24 h and then irradiated with a 1064-nm laser at a power density of 2.0 W/cm^2 on an ice box for 10 min. In contrast, for in vitro PTT experiments, 50 μL of sodium azide (10 μM) was added to cells that had been previously incubated with $Cu_2(OH)$-$PO_4@PAA$ (250 μg/mL) for 24 h, and these cells were then irradiated with a 1064-nm laser at a power density of 2.0 W/cm^2 for 10 min. For in vitro PDT/PTT combined experiments, HeLa cells seeded in 96-well plates were incubated with $Cu_2(OH)PO_4@PAA$ (250 μg/mL) for 24 h and then irradiated with a 1064-nm laser at a power density of 2.0 W/cm^2 for 10 min. Finally, the MTT assay was used to determine the relative cell viabilities.

2.8. In Vitro Phototherapeutic Effect. To evaluate the phototherapeutic effects at the cellular level, HeLa cells were first incubated in a 35-mm quartz cuvette at a density of 3×10^5 cells per dish and allowed to grow for 24 h at 37 °C until they approached overgrowth. Then, 2.0 mL of medium containing $Cu_2(OH)PO_4@PAA$ (250 μg/mL) was added to the cuvette to replace the culture medium. After incubation for another 24 h, the cells were rinsed three times with PBS to remove the nonspecifically adsorbed or residual nanoparticles in the medium. Then , the cells were irradiated with a 1064-nm laser for different time intervals (2, 4, 6, and 10 min). Finally, the irradiated cells were rinsed with PBS and stained with calcein AM and PI. The stained cells were immediately measured with an Olympus BX53 fluorescence microscope.

2.9. In Vivo Antitumor Effect. Female BALB/C nude mice (5 weeks, 18−22 g) were obtained from Vital River Experimental Animal Technology Co., Ltd. (Beijing), and all of the in vivo experiments were implemented according to the crieria of the National Regulation of China for the Care and Use of Laboratory Animals. First, the tumors were inoculated by subcutaneous injection of 1×10^7 HeLa cells in the left flank of each BALB/c mouse using 50% matrigel. After 2 weeks of growth, the tumor size reached about 200 mm^3. Then, the tumor-bearing nude mice were randomized into five groups ($n = 5$, each group), and 100 μL of PBS or $Cu_2(OH)PO_4@PAA$ (1 mg/mL) solution was intratumorally injected into the mice. The five groups are as follows: (1) control group receiving only PBS injection, (2) group

receiving $Cu_2(OH)PO_4@PAA$ injection, (3) group receiving NIR irradiation for 10 min, and (4,5) groups treated with $Cu_2(OH)PO_4@$ PAA injection and 1064-nm NIR irradiation for (4) 5 and (5) 10 min. The power density of the NIR laser was 2 W/cm^2, and the treatment began 2 h after the intratumoral injection. The phototherapeutic efficiency of each group was evaluated by measuring the tumor volumes, expressed as $V = \text{length} \times \text{width}^2$. Relative tumor volumes were calculated as V/V_0, where V_0 represents the tumor volume when the treatment was just initiated. Relative body weight was calculated as W/W_0, where W_0 corresponds to the mouse's weight when the treatment was just initiated.

2.10. Histology Analyses. Histology analysis was performed at the 14th day after treatment. The tumor tissues and major organs including liver, kidney, heart, lung, and spleen from the control and treated groups were isolated, fixed in 4% paraformaldehyde solution, and embedded in paraffin. The sliced tumor tissues and organs were stained with hematoxylin and eosin (H&E) and examined with an Olympus BX53 fluorescence microscope (Olympus, Tokyo, Japan).

3. RESULTS AND DISCUSSION

In this work, $Cu_2(OH)PO_4$ nanoparticles were fabricated by a hydrothermal process in which PAA was introduced for surface modification and size control. Figure 1a,b displays TEM images of obtained sample, which was observed as many monodisperse quantum dots (QDs) with an average particle size of about 4 nm (Figure 1c). The effective hydrodynamic diameter of the $Cu_2(OH)PO_4@PAA$ QDs was 10.5 nm, on average. The increase in hydrodynamic diameter is attributed to the linkage of the PAA polymer to the surface of the $Cu_2(OH)PO_4$ QDs and the formation of a surface hydration layer (Figure S1). We next checked the crystal nature of the sample by the XRD method. As shown in Figure 1d, all of the reflective peaks could be definitely indexed to JCPDS file no. 360404, and no impurities were found, indicating that a pure crystal phase of $Cu_2(OH)PO_4$ was successfully obtained. For comparison, we

also synthesized $Cu_2(OH)PO_4$ without adding PAA, while keeping other experimental parameters unchanged. This confirmed that PAA plays an important role in confining the particle dimensions, as evidenced by the microsized and irregular-shaped particles for $Cu_2(OH)PO_4$ without addition of PAA (Figure S2). It is worth mentioning that $Cu_2(OH)PO_4$ samples show size-dependent photoabsorption properties. The absorption intensity increases with the decrement of the $Cu_2(OH)PO_4$ particle size in the desired biological window of 100−1400 nm (Figure S3). FT-IR analysis was then performed to confirm whether the $Cu_2(OH)PO_4$ QDs were decorated with PAA ligands. For the $Cu_2(OH)PO_4$ QDs, the peaks at 2975 and 2928, 1715, 1585, and 1408 cm^{-1} were attributed to the C−H stretching vibration mode, the C=O stretching vibration mode, and the O−H bending vibration mode, respectively, all of which should come from the PAA ligand.[43,44]

Compared with the spectrum of pure PAA, the slight shift in the O−H mode might result from the formation of P−OH between $Cu_2(OH)PO_4$ and PAA. In addition, the absorption at 1048 cm^{-1} of $Cu_2(OH)PO_4$ QDs is typical character of phosphate ion from $Cu_2(OH)PO_4$ part.[45] Consequently, the FT-IR results verified that the composition of the $Cu_2(OH)PO_4$ QDs could be exactly expressed as $Cu_2(OH)PO_4@PAA$. Afterward, we employed thermogravimetric analysis to determine the quantity of PAA present on the $Cu_2(OH)PO_4$. In Figure 1d, both the pure $Cu_2(OH)PO_4$ control and $Cu_2(OH)PO_4@PAA$ show a sharp weight loss at 560 °C as a result of $Cu_2(OH)PO_4$ thermal decomposition. In this work, we assumed that the weight difference between $Cu_2(OH)PO_4$ and $Cu_2(OH)PO_4@PAA$ at 550 °C, which is temperature just lower than thermal decomposition temperature, is the weight percentage of PAA modification layer. In this way, the content of PAA in $Cu_2(OH)PO_4@PAA$ was determined as 6.09%.

Then, the optical absorption properties and photothermal conversion ability of $Cu_2(OH)PO_4@PAA$ QDs were surveyed. Figure 2a shows the powder absorbance of $Cu_2(OH)PO_4@$ PAA QDs, in which a broad absorption band ranging from 500 to 1600 nm can be discerned. Its maximum absorption platform is in the range of 800−1300 nm, thereby fully covering biological windows I (750−950 nm) and II (1000−1300 nm). Subsequently, we measured the photoabsorption of aqueous $Cu_2(OH)PO_4@PAA$ QD dispersions with various concentrations. We found that the absorption increased with the concentration of $Cu_2(OH)PO_4@PAA$ QDs at all wavelengths, especially in the NIR region, further demonstrating the photoabsorption ability of $Cu_2(OH)PO_4@PAA$ QDs. On the basis of the above results, a desirable photothermal conversion effect of $Cu_2(OH)PO_4@PAA$ QD dispersions can reasonably be anticipated. As shown in Figure 2c,d, the increase in the temperature of pure water under 1064-nm laser irradiation was about 6 °C after 10 min, whereas this increase could be obviously enhanced by the introduction of $Cu_2(OH)PO_4@$ PAA QDs. The more $Cu_2(OH)PO_4@PAA$ QDs present, the higher the temperature increment was. Therefore, the $Cu_2(OH)PO_4@PAA$ QDs of this work satisfy the basic essential requirements for implementing PTT.

PDT is a type of therapeutic approach that relies on the photogeneration of ROS (in most cases, singlet oxygen) to induce the apoptosis of tumor cells. Therefore, to check the possibility of using $Cu_2(OH)PO_4@PAA$ as a photosensitizer for executing PDT, the photosensitive formation of ROS was examined. First, we inspected the ROS level under 1064-nm irradiation in aqueous solution. For this purpose, we used the
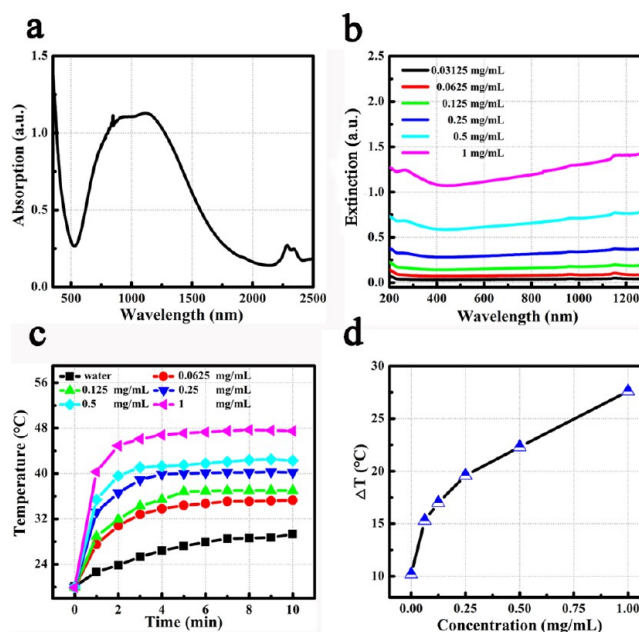
Figure 2. Photoabsorption and photothermal properties of $Cu_2(OH)$-$PO_4@PAA$. (a) Powder absorption spectrum of $Cu_2(OH)PO_4@PAA$. (b) Extinction spectra of $Cu_2(OH)PO_4@PAA$ aqueous suspensions with different concentrations. (c) Temperature elevation of $Cu_2(OH)$-$PO_4@PAA$ aqueous suspensions under 1064-nm laser irradiation as a function of irradiation time (power density = 2.0 W/cm^2). (d) Temperature change after 10 min of irradiation as a function of $Cu_2(OH)PO_4@PAA$ concentration.

ROS indicator DPBF, which is a compound that has a characteristic absorption peak at 410 nm. It is readily decomposed by singlet oxygen ($^1O_2$), thus leading to a decrease of the optical absorption at 410 nm.[46] Accordingly, a spectrophotometric method can be employed to determine the degree of $^1O_2$ production. As shown in Figure 3a, the test $Cu_2(OH)PO_4@PAA$ dispersion exhibited a marked and rapid decrement in the optical absorbance of DPBF as compared to that of pure water, indicating the excellent photosensitive ability of $Cu_2(OH)PO_4@PAA$ to generate singlet oxygen under NIR irradiation in aqueous solution. As can be seen from Figure S4, $Cu_2(OH)PO_4@PAA$ QDs can produce ROS under laser illumination at three different wavelengths. However, compared with the results observed at theother two wavelengths (808 and 880 nm), $Cu_2(OH)PO_4@PAA$ QDs can produce a higher ROS level under illumination with a 1064-nm laser, which is due to their stronger absorption at 1064 nm.

To go a step further, we next inspected the intracellular production of ROS within HeLa cells by $Cu_2(OH)PO_4@PAA$ under irradiation. Visualization of the ROS signal was realized with a probe of H_2DCFDA, which is a cell-permeable molecule without fluorescence but can be convert into fluorescent 2′,7′-dichloroflorescein with a brilliant green emission when oxidized by $^1O_2$. Consequently, the evaluation of intracellular ROS generation with this probe can be achieved by the observation of fluorescence. In this set of experiments, H_2O_2-treated HeLa cells were used as a positive control. In Figure 3b−d, no green fluorescence can be observed for the control group without any treatment or for the $Cu_2(OH)PO_4@PAA$-treated group, and only sporadic spots of green light can be observed for the NIR-irradiated group. In sharp contrast, strong and extensive green fluorescence emerged in the H_2O_2 positive control and in group
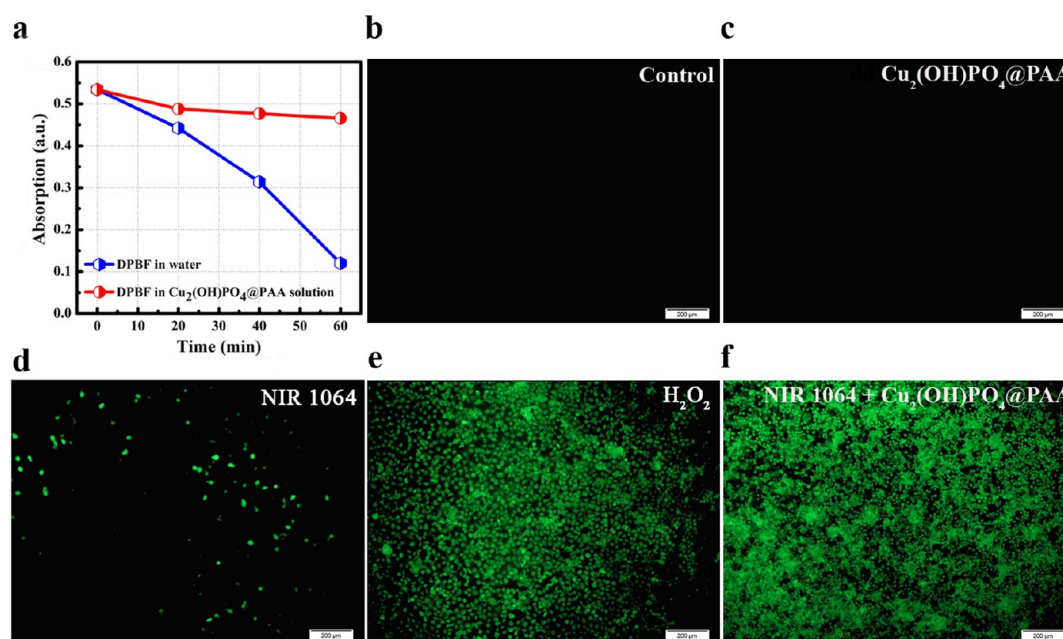
Figure 3. Detection of ROS production by NIR-light-irradiated $Cu_2(OH)PO_4$@PAA. (a) Absorption spectra of DPBF in water and in a $Cu_2(OH)PO_4$@PAA dispersion after different irradiation times. (b−f) Fluorescence microscope images of ROS generation in HeLa cells receiving different treatments (NIR laser, 2 W/cm^2, 10 min; scale bar = 200 μm).

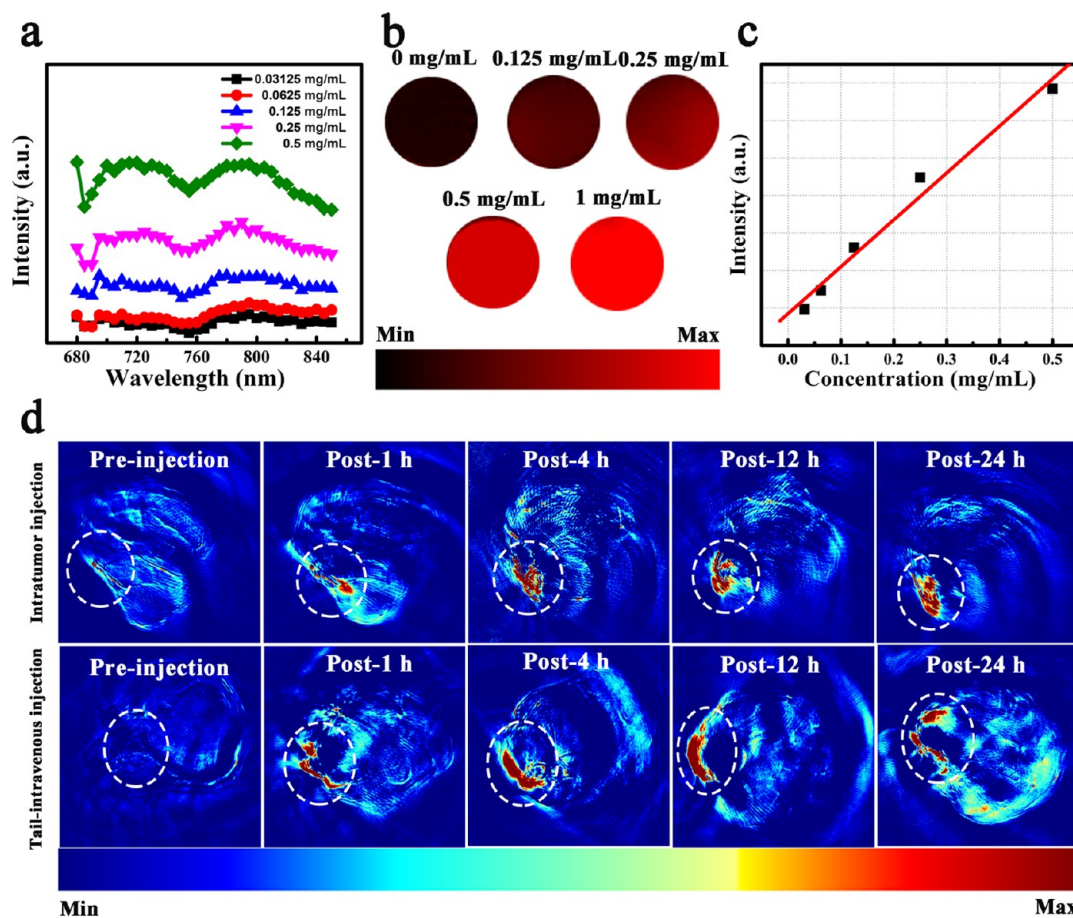**Figure 4.** In vitro and in vivo PAT imaging. (a) PAT phantom signals and (b) images of $Cu_2(OH)PO_4$@PAA solutions with different concentrations. (c) Plot of photoacoustic signal versus $Cu_2(OH)PO_4$@PAA concentration. (d) In vivo PAT images of HeLa tumor-bearing mice before and at different times after intratumoral or intravenous injection of $Cu_2(OH)PO_4$@PAA. Tumor sites are marked with dashed circles.
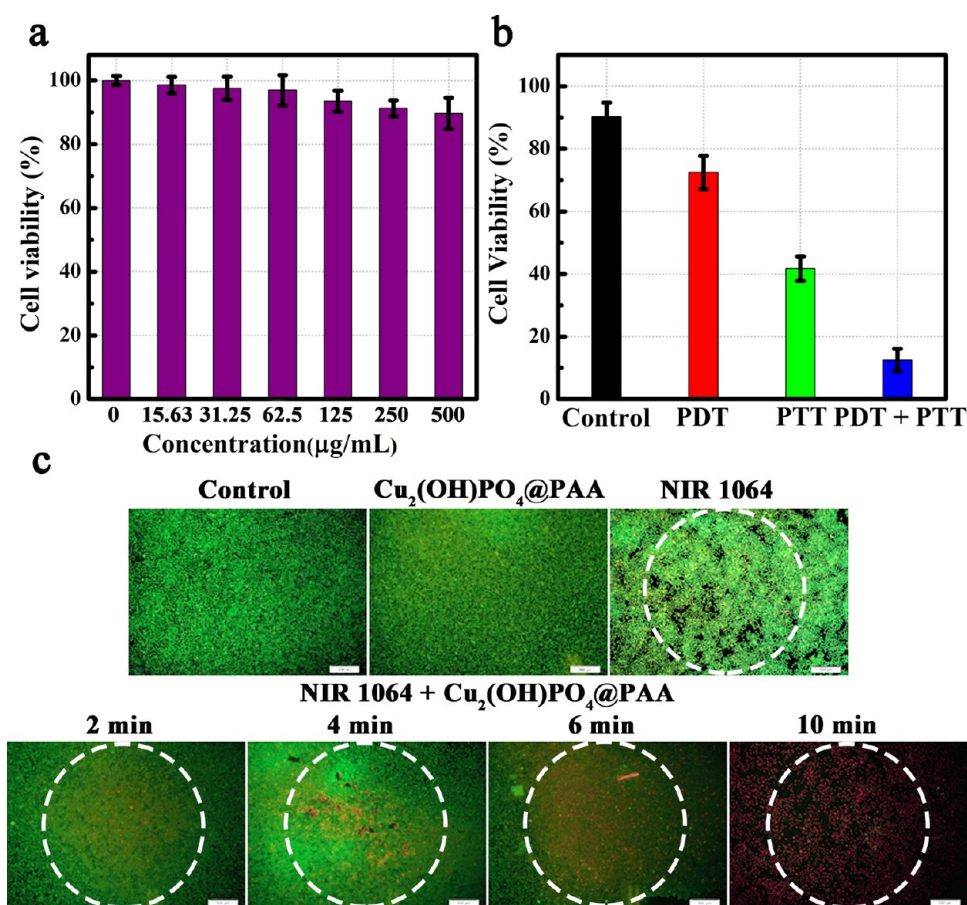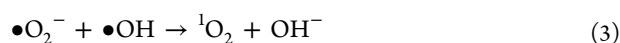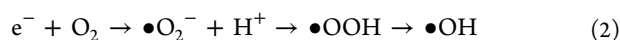
Figure 5. In vitro cytotoxicity assay and phototherapy effect of $Cu_2(OH)PO_4$@PAA. (a) Cell viability after coincubation with $Cu_2(OH)PO_4$@PAA at different concentrations. (b) Relative cell viability after different treatments with $Cu_2(OH)PO_4$@PAA. (c) In vitro phototherapy study of $Cu_2(OH)PO_4$@PAA.

treated with both $Cu_2(OH)PO_4$@PAA and NIR irradiation, thus illustrating that NIR-light-irradiated $Cu_2(OH)PO_4$@PAA can produce sufficient ROS even within cancer cells. To further confirm intracellular ROS production by NIR irradiation combined with $Cu_2(OH)PO_4$@PAA QDs, corresponding flow cytometry measurements were carried out. As can be seen in Figure S5, unlike for the three control groups (Figure S5a−c), the flow cytometry results showed a spectral shift of the fluorescence intensity curves to the right after 1064-nm NIR activation of the $Cu_2(OH)PO_4$@PAA QDs (Figure S5d), indicating a significant increment of the intracellular ROS level in the HeLa cells. $Cu_2(OH)PO_4$ has been reported to be a good near-infrared-activated photocatalyst that can produce free electrons and subsequently facilitate formation of ROS under NIR light irradiation ($\lambda > 800$ nm). Based on this discovery, we implemented the PDT effect using $Cu_2(OH)PO_4$ under NIR irradiation. In accordance with previous related works,[8,35,47] a possible mechanism for ROS generation under NIR laser irradiation might be as follows

$$Cu^{2+} + hv \rightarrow Cu^{3+} + e^- \tag{1}$$

$$e^- + O_2 \rightarrow \bullet O_2^- + H^+ \rightarrow \bullet OOH \rightarrow \bullet OH \tag{2}$$

$$\bullet O_2^- + \bullet OH \rightarrow {}^1O_2 + OH^- \tag{3}$$

$$Cu^{3+} + OH^- \rightarrow Cu^{2+} + \bullet OH \tag{4}$$

Photoacoustic tomography (PAT) imaging is a new emerging imaging modality with merits of high spatial resolution, noninvasiveness, deep penetration, and a capability for guiding bulk tumor resection intraoperatively.[31] The image-forming principle of PAT relies on the measurement of ultrasonic waves produced by a biological tissue or a PAT contrast agent upon laser irradiation to induce a photothermal phenomenon. However, most pathological tissues are not ideal endogenous PAT contrast because of ir the inferior photo-absorption. Hence, exogenous NIR absorption nanomaterials are often required for in vivo PAT imaging. As mentioned previously, $Cu_2(OH)PO_4$@PAA QDs with high photoabsorp-tion and excellent photothermal effects meet the essential requirements for exogenous PAT contrast. We first studied the photoacoustic response of $Cu_2(OH)PO_4$@PAA solutions at different concentrations, which clearly presented a dose-dependent signal intensity (see Figure 4a−c). The photoacoustic signals could be detected over the whole range of tested wavelengths (680−850 nm) and were enhanced with $Cu_2(OH)PO_4$@PAA concentration in PAT phantom images. A linear correlation was found between the concentration of $Cu_2(OH)PO_4$@PAA QDs and the photoacoustic (PA) signals at 800 nm (Figure 4c). Motivated by the above in vitro PAT results, we next employed the $Cu_2(OH)PO_4$@PAA QDs for in vivo tumor imaging. HeLa tumor-bearing mice were selected and injected with $Cu_2(OH)PO_4$@PAA QDs (100 μL, 2 mg mL^{-1}) by intratumor injection or intravenous injection. Then, we kept track of the PAT signal from the tumor site for 24 h
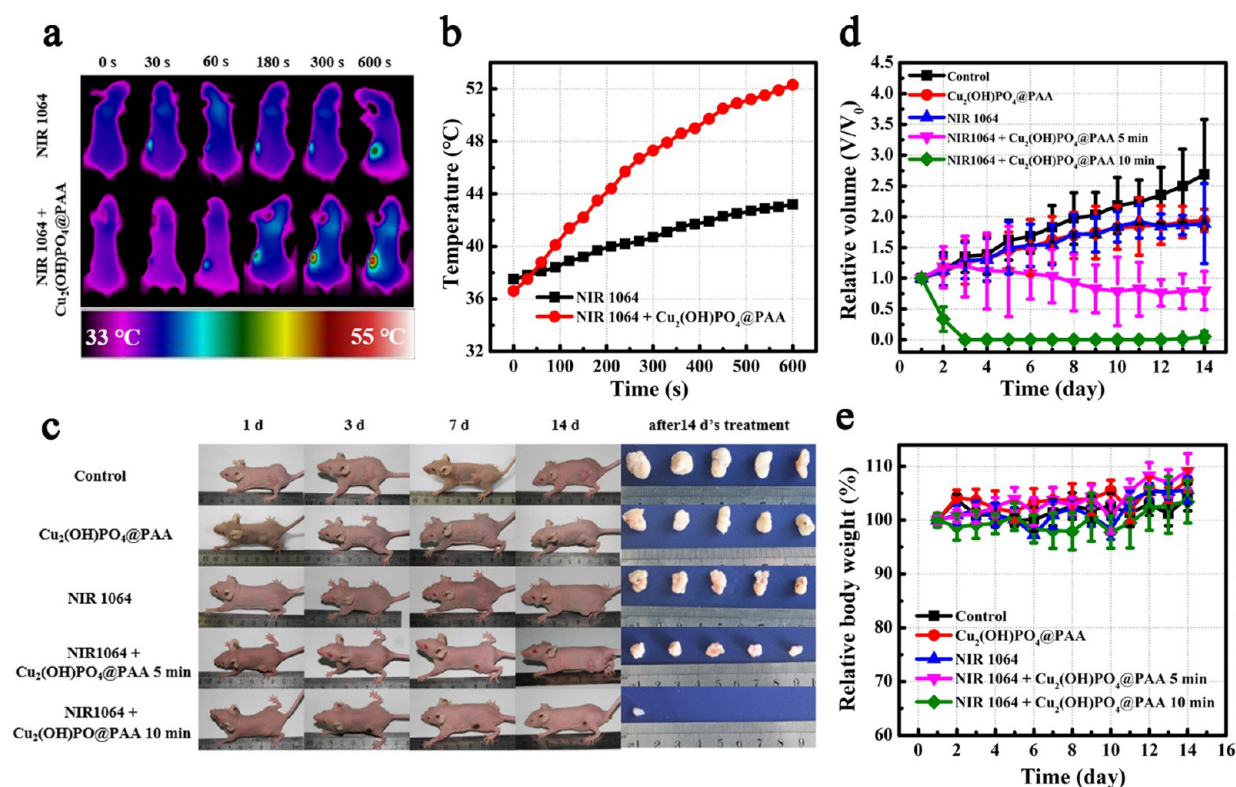
Figure 6. In vivo phototherapy. (a) Thermographic images of HeLa tumor-bearing mice under 1064-nm laser irradiation. (b) Temperature variation of tumors depicted in panel a. (c) Representative photographs of mice and tumors during the treatments. (d,e) Quantitative measurements of (d) tumor volume and (e) body weight of mice after various treatments.

after injection. As displayed in Figure 4d, there was no PA signal or at least a very weak signal at the tumor site before $Cu_2(OH)PO_4@PAA$ QD injection, suggesting that the cancer tissue itself is incapable of forming a PAT image. For the group subjected to the intratumoral injection of $Cu_2(OH)PO_4@PAA$ QDs, PAT signals from the tumor site can be clearly discerned throughout the whole observation time of 24 h, and the area in which PA signals are observed is enlarged with time but is always confined to the tumor site, suggesting the long-term retention of $Cu_2(OH)PO_4@PAA$ QDs at the tumor site upon intratumoral injection. For the group subjected to tail intravenous injection, a passive targeting effect by enhanced permeability and retention (EPR) also made the tumor site clearly discernable; however, the spreading of the $Cu_2(OH)$-$PO_4@PAA$ QDs from the tumor site to other tissue occurred 24 h after injection. Therefore, in this work, all subsequent in vivo phototherapy was carried out by means of intratumoral injection. Nevertheless, we can also conclude that $Cu_2(OH)$-$PO_4@PAA$ QDs can function as a potential PA contrast agent for in vivo tumor imaging.

The cytotoxicity of the $Cu_2(OH)PO_4@PAA$ QDs is significant for determining their potential in antitumor applications. To be qualified, a phototherapy agent should be highly biocompatible in the absence of laser irradiation but exhibit controllable cytotoxicity when exposed to light irradiation. Prior to phototherapy, the in vitro cytotoxicity of the $Cu_2(OH)PO_4@PAA$ QDs against HeLa cells was studied by means of the standard MTT assay in the absence of laser irradiation (Figure 5a). It was found that the $Cu_2(OH)PO_4@$ PAA QDs have an insignificant cytotoxic effect toward HeLa cells at concentrations up to 500 μg/mL (Figure 5a). Then, the $Cu_2(OH)PO_4@PAA$ QDs were used as a phototherapy agent

for in vitro cancer cell ablation under NIR light irradiation. In this case, $Cu_2(OH)PO_4@PAA$ QDs can produce hyperthermia and ROS simultaneously upon NIR irradiation and result in a synergistic PDT/PTT effect on cancer cells. To distinguish the roles of PDT and PTT in contributing to the overall therapeutic effect, two control experiments were performed. In the first experiment, examining PTT alone, cell viability was measured after treatment with the singlet-oxygen quencher sodium azide; hence, the PDT effect was deemed to be eliminated, and the phototherapeutic effect was considered to originate only from the PTT contribution.[48] In contrast, in the second, PDT-only experiment, the phototherapy treatment was performed at a chamber temperature of 4 °C, so that the temperature of the irradiation area never exceeded 20 °C and the light-irradiation-induced photothermal ablation was greatly suppressed; thus, in this case, the therapeutic effect reflected only the PDT contribution. MTT assays were also performed to quantitatively measure the relative cell viabilities after different treatments. As shown in Figure 5b, for the single therapeutic effects of PDT and PTT alone, the cancer cell inhibition rates were just 27.6% and 58.3%, respectively, under 1064-nm NIR irradiation. In sharp contrast, the cell-killing efficiency markedly enhanced to greater than 85% for the combined PDT/PTT therapy. Therefore, it is known that these two types of phototherapy methods can provide mutual promotion and that the combination of PDT and PTT can give rise to a dramatic synergistic effect to destroy cancer cells. On the basis of the above results, the phototherapeutic effect of $Cu_2(OH)PO_4@PAA$ QDs under NIR light irradiation was further checked by the fluorescent visualization of a photo-ablation-induced live−dead assay. Toward this end, calcein AM with a green fluorescent response for labeling living cells and
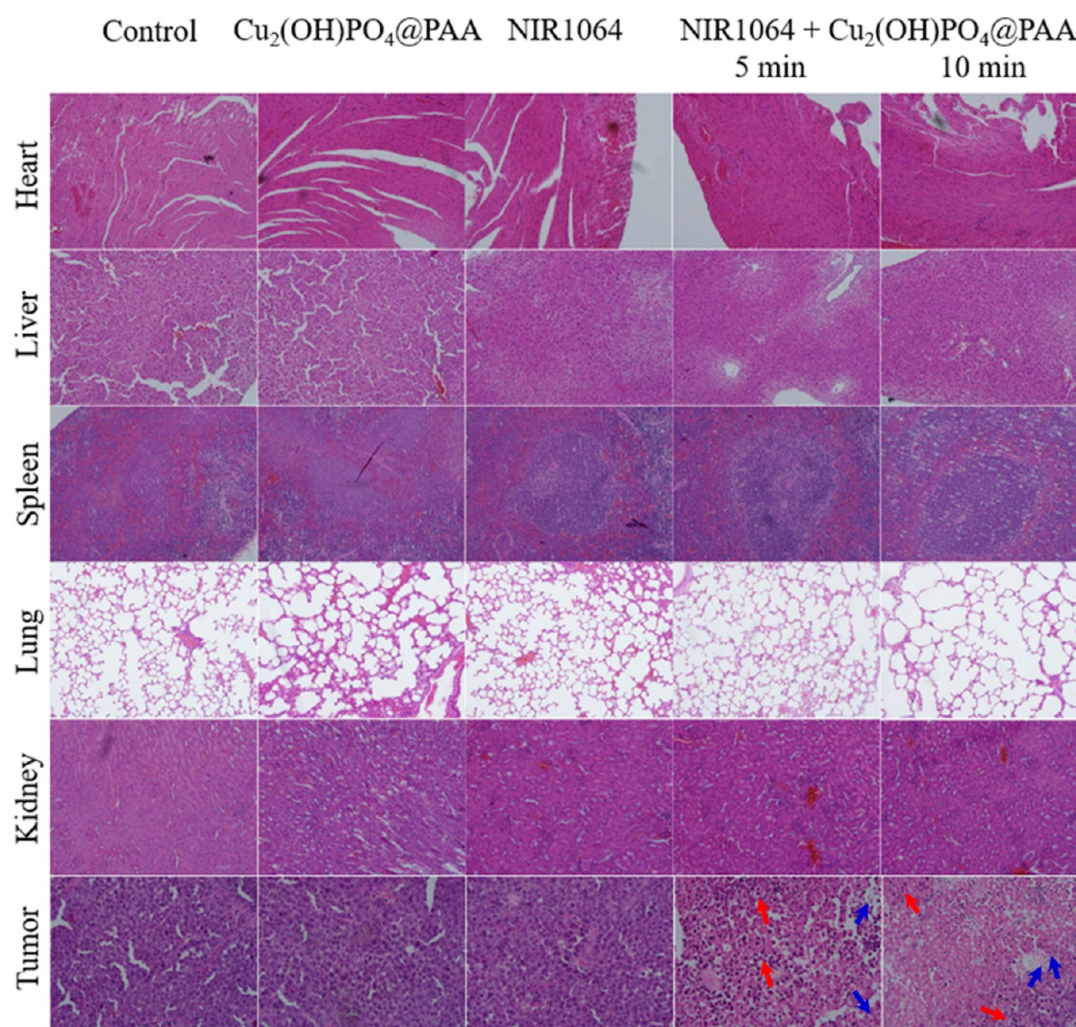
Figure 7. Histology staining of major organ slices (liver, kidney, heart, lung, and spleen) and tumor slices collected from different groups of mice after 14 days of treatment.

propidium (PI) with a red fluorescent response for labeling dead HeLa cells were employed. As shown in Figure 5c, the control group without any treatment and the groups treated with $Cu_2(OH)PO_4$@PAA QDs alone and with NIR irradiation alone emitted only a bright green color, suggesting negligible cancer cell death. In striking contrast, the cells treated with $Cu_2(OH)PO_4$@PAA QDs in combination with 1064-nm laser irradiation showed red fluorescence from the irradiated site. With increasing irradiation time, the area containing dead cells enlarged prominently, indicating the NIR-irradiation-mediated phototherapy effect of $Cu_2(OH)PO_4$@PAA QD.

Encouraged by the above positive in vitro results, we next investigated the in vivo phototherapeutic effect on HeLa tumor-bearing nude mice. First, the increases in temperature of the mice tumor sites upon NIR irradiation were monitored with an infrared camera. Panels a and b of Figure 6 show the time-dependent thermographic images and temperature rising curves, respectively, for mice treated with PBS or $Cu_2(OH)$-PO_4@PAA QDs. Obviously, $Cu_2(OH)PO_4$@PAA-QD-mediated group exhibited a much higher hyperthermia effect, and the maximum temperature after 10 min of irradiation reached 52.4 °C, which is high enough to induce irreversible damage to the cancer tissue. It has been reported that even just a short-time exposure (about 5 min) of cancer tissue to hyperthermia

above 48 °C can induce massive cancer destruction.[49] With the above results in hand, we subsequently evaluated the in vivo phototherapeutic effect. Tumor-bearing nude mice with tumor volumes of about 200 mm^3 were randomly divided into five groups ($n = 5$, each group): (1) control group receiving no treatment, (2) group treated with $Cu_2(OH)PO_4$@PAA QDs, (3) group subjected to 10 min of NIR irradiation, (4) group treated with $Cu_2(OH)PO_4$@PAA QDs and subjected to 5 min of NIR irradiation, and (5) group treated with $Cu_2(OH)PO_4$@PAA QDs and subjected to 10 min of NIR irradiation. The antitumor efficiency was evaluated by measuring the average tumor size in the following 2 weeks after the treatments. As shown in Figure 6c,d, the tumors in the control group and the groups treated with $Cu_2(OH)PO_4$@PAA QDs alone and with NIR irradiation alone kept growing all the time, demonstrating no obvious inhibition of tumor growth by $Cu_2(OH)PO_4$@PAA QDs alone or by NIR irradiation alone. In contrast, for the phototherapeutic groups receiving $Cu_2(OH)PO_4$@PAA QDs plus 1064-nm irradiation, the treatment greatly suppressed tumor progression, especially for the group with the longer exposure duration of 10 min, in which the tumors of four of the five mice were completely removed by the photoablation process. Moreover, the body weights of the mice in the different groups indicated no weight loss or notable changes

throughout the whole process, suggesting minimal invasion of the mice by this phototherapy for oncotherapy.

Finally, we studied the antitumor mechanism and potential biological toxicity risk of $Cu_2(OH)PO_4$@PAA QDs by a hematoxylin and eosin (H&E) staining analysis. The major organs, such as heart, kidney, liver, spleen, and lung, exhibited no appreciable lesions in the sections of the tissues (Figure 7), thus implying that the application of $Cu_2(OH)PO_4$@PAA QDs for combination PDT/PTT therapy is of high biological safety. The histology staining of the tumor slices indicated massive cancer cellular necrosis and apoptosis in the phototherapy group, particularly in the group subjected to irradiation for a longer time, which can be reasonably attributed to a synergistic effect of PDT/PTT treatment.

At present, nearly all types of imaging-guided therapy formulations are in the proof-of-concept phase and have not actually been applied in clinical practice yet. Clinical application will be realized when PAT imaging technology is mature enough for humans and PAT imaging equipment are equipped with NIR lasers. If this happens, imaging-guided therapy could be implemented in the following way. First, the theranostic agent, for example, $Cu_2(OH)PO_4$@PAA QDs, is delivered to the site of the tumor (such as mammary cancer or melanoma). Next, the distribution and enrichment of the theranostic agent in the tumor can be observed under an imaging model so that the best treatment time can be determined. Then, the NIR laser is pulsed to treat the tumor by PTT/PDT treatment, and PAT imaging can be used to monitor the whole therapeutic process. Moreover, the PAT imaging model can also be used to observe the metabolic process of the theranostic agent.

4. CONCLUSIONS

In this work, we have fabricated the $Cu_2(OH)PO_4$ quantum dots for use in a multipurpose cancer theranostic system embracing the photoacoustic imaging modality and the combination of PDT and PTT phototherapy. As revealed by optical measurements, $Cu_2(OH)PO_4$ quantum dots can harvest a wide spectrum of NIR light, benefiting both local hyperthemia and ROS generation upon NIR irradiation, thus realizing synergetic PTT/PDT therapeutic effects. We employed in vitro cell experiments to confirm the individual functions of PTT and PTT, as well as the combined PDT/PTT effect, which confirmed the dual actions of $Cu_2(OH)_2PO_4$ as both a photothermal agent and a photosensitizer. Meanwhile, studies of the in vivo antitumor effect performed on tumor-bearing mice clearly illustrated the success of the inhibition or even full ablation of solid tumors using $Cu_2(OH)PO_4$-mediated phototherapy through the induction of tumor necrosis and apoptosis. What is exciting is that this method resulted in no or negligible invasion of the major organs of the mice, as verified by H&E analysis, demonstrating the great potential of $Cu_2(OH)PO_4$ for the photoablation of tumors. Furthermore, $Cu_2(OH)PO_4$ is also applicable for the in vivo PA imaging of tumor sites through either intratumor injection or tail intravenous injection to realize an imaging-guided therapeutic process. As a consequence, we have created a "three-in-one" multifunctional theranostic platform with just the single material of $Cu_2(OH)PO_4$.

ASSOCIATED CONTENT

Supporting Information

The Supporting Information is available free of charge on the ACS Publications website at DOI: 10.1021/acsami.6b15703.

Figures showing the characterization of $Cu_2(OH)PO_4$ synthesized without addition of PAA and $Cu_2(OH)PO_4$@PAA, size-dependent UV−vis−NIR absorption spectra, and results of the ROS production behavior study (PDF)

AUTHOR INFORMATION

Corresponding Authors
*E-mail: chongshenguo@hit.edu.cn.
*E-mail: shaoqinliu@hit.edu.cn.

ORCID
Chongshen Guo: 0000-0002-8000-7434

Author Contributions
W.G. and Z.Q. contributed equally. W.G. and Z.Q. conducted most of the experiments. C.G. and S.L. supervised the overall research work. D.D., T.L., F.W., J.S., and N.Z. did part of work on in vivo mice experiments. All authors have given approval to the final version of manuscript.

Notes
The authors declare no competing financial interest.

ABBREVIATIONS

PA = photoacoustic
PAA = poly(acrylic acid)
PAT = photoacoustic tomography
PDT = photodynamic therapy
PS = photosensitizer
PTT = photothermal therapy
QD = quantum dots
ROS = reactive oxygen species

REFERENCES

(1) Guo, W.; Guo, C. S.; Zheng, N. N.; Sun, T. D.; Liu, S. Q. Cs_xWO_3 Nanorods Coated with Polyelectrolyte Multilayers as a Multifunctional Nanomaterial for Bimodal Imaging-Guided Photothermal/Photodynamic Cancer Treatment. *Adv. Mater.* **2017**, *29*, 1604157.

(2) Guo, W.; Yang, C.; Lin, H.; Qu, F. Y. P(EO-*co*-LLA) Functionalized Fe_3O_4@$mSiO_2$ Nanocomposites for Thermo/pH Responsive Drug Controlled Release and Hyperthermia. *Dalton Trans.* **2014**, *43*, 18056−18065.

(3) Yang, C. Y.; Guo, W.; Cui, L. R.; An, N.; Zhang, T.; Lin, H. M.; Qu, F. Y. pH-Responsive Magnetic Core-Shell Nanocomposites for Drug Delivery. *Langmuir* **2014**, *30*, 9819−9827.

(4) Sun, X.; Huang, X.; Yan, X.; Wang, Y.; Guo, J.; Jacobson, O.; Liu, D.; Szajek, L. P.; Zhu, W.; Niu, G.; Kiesewetter, D. O.; Sun, S.; Chen, X. Chelator-Free ^{64}Cu-Integrated Gold Nanomaterials for Positron Emission Tomography Imaging Guided Photothermal Cancer Therapy. *ACS Nano* **2014**, *8*, 8438−8446.

(5) Li, S.; Xu, L. G.; Ma, W.; Wu, X. L.; Sun, M. Z.; Kuang, H.; Wang, L. B.; Kotov, N. A.; Xu, C. L. Dual-Mode Ultrasensitive Quantification of MicroRNA in Living Cells by Chiroplasmonic Nanopyramids Self-Assembled from Gold and Upconversion Nanoparticles. *J. Am. Chem. Soc.* **2016**, *138*, 306−312.

(6) Gong, H.; Dong, Z. L.; Liu, Y. M.; Yin, S. N.; Cheng, L.; Xi, W. Y.; Xiang, J.; Liu, K.; Li, Y. G.; Liu, Z. Engineering of Multifunctional Nano-Micelles for Combined Photothermal and Photodynamic

Therapy Under the Guidance of Multimodal Imaging. *Adv. Funct. Mater.* **2014**, *24*, 6492−6502.

(7) Guo, C. S.; Yu, H. J.; Feng, B.; Gao, W. D.; Yan, M.; Zhang, Z. W.; Li, Y. P.; Liu, S. Q. Highly Efficient Ablation of Metastatic Breast Cancer Using Ammonium-Tungsten-Bronze Nanocube as a Novel 1064 nm-Laser-Driven Photothermal Agent. *Biomaterials* **2015**, *52*, 407−416.

(8) Yan, M.; Li, G. L.; Guo, C. S.; Guo, W.; Ding, D. D.; Zhang, S. H.; Liu, S. Q. WO_{3-x} Sensitized TiO_2 Spheres with Full-Spectrum-Driven Photocatalytic Activities from UV to Near Infrared. *Nanoscale* **2016**, *8*, 17828−17835.

(9) Li, G. L.; Zhang, S. H.; Guo, C. S.; Liu, S. Q. Absorption and Electrochromic Modulation of Near-Infrared Light: Realized by Tungsten Suboxide. *Nanoscale* **2016**, *8*, 9861−9868.

(10) Lal, S.; Clare, S. E.; Halas, N. J. Nanoshell-Enabled Photothermal Cancer Therapy: Impending Clinical Impact. *Acc. Chem. Res.* **2008**, *41*, 1842−1851.

(11) Bardhan, R.; Lal, S.; Joshi, A.; Halas, N. J. Theranostic Nanoshells: From Probe Design to Imaging and Treatment of Cancer. *Acc. Chem. Res.* **2011**, *44*, 936−946.

(12) Peng, J. J.; Zhao, L. Z.; Zhu, X. J.; Sun, Y.; Feng, W.; Gao, Y. H.; Wang, L. Y.; Li, F. Y. Hollow Silica Nanoparticles Loaded with Hydrophobic Phthalocyanine for Near-Infrared Photodynamic and Photothermal Combination Therapy. *Biomaterials* **2013**, *34*, 7905−7912.

(13) Lin, L. S.; Cong, Z. X.; Cao, J. B.; Ke, K. M.; Peng, Q. L.; Gao, J. H.; Yang, H. H.; Liu, G.; Chen, X. Y. Multifunctional $Fe_3O_4@$Polydopamine Core-Shell Nanocomposites for Intracellular mRNA Detection and Imaging-Guided Photothermal Therapy. *ACS Nano* **2014**, *8*, 3876−3883.

(14) Lv, R. C.; Zhong, C. N.; Li, R. M.; Yang, P. P.; He, F.; Gai, S. L.; Hou, Z. Y.; Yang, G. X.; Lin, J. Multifunctional Anticancer Platform for Multimodal Imaging and Visible Light Driven Photodynamic/Photothermal Therapy. *Chem. Mater.* **2015**, *27*, 1751−1763.

(15) Zhou, M.; Zhang, R.; Huang, M.; Lu, W.; Song, S.; Melancon, M. P.; Tian, M.; Liang, D.; Li, C. A Chelator-Free Multifunctional [^{64}Cu]CuS Nanoparticle Platform for Simultaneous Micro-PET/CT Imaging and Photothermal Ablation Therapy. *J. Am. Chem. Soc.* **2010**, *132*, 15351−15358.

(16) Wang, X.; Wang, C.; Cheng, L.; Lee, S. T.; Liu, Z. Noble Metal Coated Single-Walled Carbon Nanotubes for Applications in Surface Enhanced Raman Scattering Imaging and Photothermal Therapy. *J. Am. Chem. Soc.* **2012**, *134*, 7414−7422.

(17) Bao, T.; Yin, W. Y.; Zheng, X. P.; Zhang, X.; Yu, J.; Dong, X. H.; Yong, Y.; Gao, F. P.; Yan, L.; Gu, Z. J.; Zhao, Y. L. One-Pot Synthesis of PEGylated Plasmonic MoO_{3-x} Hollow Nanospheres for Photoacoustic Imaging Guided Chemo-Photothermal Combinational Therapy of Cancer. *Biomaterials* **2016**, *76*, 11−24.

(18) Guo, M.; Huang, J.; Deng, Y. B.; Shen, H.; Ma, Y. F.; Zhang, M. X.; Zhu, A. J.; Li, Y. L.; Hui, H.; Wang, Y. Y.; Yang, X. L.; Zhang, Z. J.; Chen, H. B. pH-Responsive Cyanine-Grafted Graphene Oxide for Fluorescence Resonance Energy Transfer-Enhanced Photothermal Therapy. *Adv. Funct. Mater.* **2015**, *25*, 59−67.

(19) Lovell, J. F.; Jin, C. S.; Huynh, E.; MacDonald, T. D.; Cao, W. G.; Zheng, G. Enzymatic Regioselection for the Synthesis and Biodegradation of Porphysome Nanovesicles. *Angew. Chem., Int. Ed.* **2012**, *51*, 2429−2433.

(20) Wang, B. K.; Yu, X. F.; Wang, J. H.; Li, Z. B.; Li, P. H.; Wang, H. Y.; Song, L.; Chu, P. K.; Li, C. Z. Gold-Nanorods-siRNA Nanoplex for Improved Photothermal Therapy by Gene Silencing. *Biomaterials* **2016**, *78*, 27−39.

(21) Guo, M.; Mao, H. J.; Li, Y. L.; Zhu, A. J.; He, H.; Yang, H.; Wang, Y. Y.; Tian, X.; Ge, C. C.; Peng, Q. L.; Wang, X. Y.; Yang, X. L.; Chen, X. Y.; Liu, G.; Chen, H. B. Dual Imaging-Guided Photothermal/Photodynamic Therapy Using Micelles. *Biomaterials* **2014**, *35*, 4656−4666.

(22) Jing, L. J.; Liang, X. L.; Deng, Z. J.; Feng, S. S.; Li, X. D.; Huang, M. M.; Li, C. H.; Dai, Z. F. Prussian Blue Coated Gold Nanoparticles for Simultaneous Photoacoustic/CT Bimodal Imaging and Photothermal Ablation of Cancer. *Biomaterials* **2014**, *35*, 5814−5821.

(23) Song, J. B.; Wang, F.; Yang, X. Y.; Ning, B.; Harp, M. G.; Culp, S. H.; Hu, S.; Huang, P.; Nie, L. M.; Chen, J. Y.; Chen, X. Y. Gold Nanoparticle Coated Carbon Nanotube Ring with Enhanced Raman Scattering and Photothermal Conversion Property for Theranostic Applications. *J. Am. Chem. Soc.* **2016**, *138*, 7005−7015.

(24) Yang, T.; Wang, Y.; Ke, H. T.; Wang, Q. L.; Lv, X. Y.; Wu, H.; Tang, Y. A.; Yang, X. L.; Chen, C. Y.; Zhao, Y. L.; Chen, H. B. Protein-Nanoreactor-Assisted Synthesis of Semiconductor Nanocrystals for Efficient Cancer Theranostics. *Adv. Mater.* **2016**, *28*, 5923−5930.

(25) Chao, Y.; Wang, G. L.; Liang, C.; Yi, X.; Zhong, X. Y.; Liu, J. J.; Gao, M.; Yang, K.; Cheng, L.; Liu, Z. Rhenium-188 Labeled Tungsten Disulfide Nanoflakes for Self-Sensitized, Near-Infrared Enhanced Radioisotope Therapy. *Small* **2016**, *12*, 3967−3975.

(26) Liu, T.; Shi, S. X.; Liang, C.; Shen, S. D.; Cheng, L.; Wang, C.; Song, X. J.; Goel, S.; Barnhart, T. E.; Cai, W. B.; Liu, Z. Iron Oxide Decorated MoS_2 Nanosheets with Double PEGylation for Chelator-Free Radio Labeling and Multimodal Imaging Guided Photothermal Therapy. *ACS Nano* **2015**, *9*, 950−960.

(27) Tian, G.; Zhang, X.; Zheng, X. P.; Yin, W. Y.; Ruan, L. F.; Liu, X. D.; Zhou, L. J.; Yan, L.; Li, S. J.; Gu, Z. J.; Zhao, Y. L. Multifunctional Rb_xWO_3 Nanorods for Simultaneous Combined Chemo-Photothermal Therapy and Photoacoustic/CT Imaging. *Small* **2014**, *10*, 4160−4170.

(28) Ku, G.; Zhou, M.; Song, S. L.; Huang, Q.; Hazle, J.; Li, C. Copper Sulfide Nanoparticles As a New Class of Photoacoustic Contrast Agent for Deep Tissue Imaging at 1064 nm. *ACS Nano* **2012**, *6*, 7489−7496.

(29) Liu, X.; Law, W. C.; Jeon, M.; Wang, X. L.; Liu, M. X.; Kim, C.; Prasad, P. N.; Swihart, M. T. $Cu_{2-x}Se$ Nanocrystals with Localized Surface Plasmon Resonance as Sensitive Contrast Agents for In Vivo Photoacoustic Imaging: Demonstration of Sentinel Lymph Node Mapping. *Adv. Healthcare Mater.* **2013**, *2*, 952−957.

(30) Wang, L. H. V.; Gao, L. Photoacoustic Microscopy and Computed Tomography: From Bench to Bedside. *Annu. Rev. Biomed. Eng.* **2014**, *16*, 155−185.

(31) Zhang, Y. M.; Jeon, M.; Rich, L. J.; Hong, H.; Geng, J. M.; Zhang, Y.; Shi, S. X.; Barnhart, T. E.; Alexandridis, P.; Huizinga, J. D.; Seshadri, M.; Cai, W. B.; Kim, C.; Lovell, J. F. Non-Invasive Multimodal Functional Imaging of the Intestine with Frozen Micellar Naphthalocyanines. *Nat. Nanotechnol.* **2014**, *9*, 631−638.

(32) Meng, Z. Q.; Wei, F.; Wang, R. H.; Xia, M. G.; Chen, Z. G.; Wang, H. P.; Zhu, M. F. NIR-Laser-Switched In Vivo Smart Nanocapsules for Synergic Photothermal and Chemotherapy of Tumors. *Adv. Mater.* **2016**, *28*, 245−253.

(33) Zheng, X. P.; Shi, J. X.; Bu, Y.; Tian, G.; Zhang, X.; Yin, W. Y.; Gao, B. F.; Yang, Z. Y.; Hu, Z. B.; Liu, X. F.; Yan, L.; Gu, Z. J.; Zhao, Y. L. Silica-Coated Bismuth Sulfide Nanorods as Multimodal Contrast Agents for a Non-Invasive Visualization of the Gastrointestinal Tract. *Nanoscale* **2015**, *7*, 12581−12591.

(34) An, F. F.; Deng, Z. J.; Ye, J.; Zhang, J. F.; Yang, Y. L.; Li, C. H.; Zheng, C. J.; Zhang, X. H. Aggregation-Induced Near-Infrared Absorption of Squaraine Dye in an Albumin Nanocomplex for Photoacoustic Tomography in Vivo. *ACS Appl. Mater. Interfaces* **2014**, *6*, 17985−17992.

(35) Wang, G.; Huang, B. B.; Ma, X. C.; Wang, Z. Y.; Qin, X. Y.; Zhang, X. Y.; Dai, Y.; Whangbo, M. H. $Cu_2(OH)PO_4$, a Near-Infrared-Activated Photocatalyst. *Angew. Chem., Int. Ed.* **2013**, *52*, 4810−4813.

(36) Feng, W.; Zhou, X. J.; Nie, W.; Chen, L.; Qiu, K. X.; Zhang, Y. Z.; He, C. L. $Au/Polypyrrole@Fe_3O_4$ Nanocomposites for MR/CT Dual-Modal Imaging Guided-Photothermal Therapy: An In Vitro Study. *ACS Appl. Mater. Interfaces* **2015**, *7*, 4354−4367.

(37) Meng, Z. Q.; Wei, F.; Wang, R. H.; Xia, M. G.; Chen, Z. G.; Wang, H. P.; Zhu, M. F. NIR-Laser-Switched In Vivo Smart Nanocapsules for Synergic Photothermal and Chemotherapy of Tumors. *Adv. Mater.* **2016**, *28*, 245−253.

(38) Wang, Y. H.; Wang, H. G.; Liu, D. P.; Song, S. Y.; Wang, X.; Zhang, H. J. Graphene Oxide Covalently Grafted Upconversion

Nanoparticles for Combined NIR Mediated Imaging and Photo-thermal/Photodynamic Cancer Therapy. *Biomaterials* **2013**, *34*, 7715−7724.

(39) Chen, R.; Wang, X.; Yao, X. K.; Zheng, X. C.; Wang, J.; Jiang, X. Q. Near-IR-Triggered Photothermal/Photodynamic Dual-Modality Therapy System via Chitosan Hybrid Nanospheres. *Biomaterials* **2013**, *34*, 8314−8322.

(40) Wang, H.; Agarwal, P.; Zhao, S. T.; Yu, J. H.; Lu, X. B.; He, X. M. Combined Cancer Therapy with Hyaluronan-Decorated Fullerene-Silica Multifunctional Nanoparticles to Target Cancer Stem-Like Cells. *Biomaterials* **2016**, *97*, 62−73.

(41) Zhang, T.; Lin, H. M.; Cui, L. R.; An, N.; Tong, R. H.; Chen, Y. H.; Yang, C. Y.; Li, X.; Qu, F. Y. NIR-Sensitive UCNP@mSiO$_2$ Nanovehicles for on-Demand Drug Release and Photodynamic Therapy. *RSC Adv.* **2016**, *6*, 26479−26489.

(42) Chen, R.; Wang, X.; Yao, X. K.; Zheng, X. C.; Wang, J.; Jiang, X. Q. Near-IR-Triggered Photothermal/Photodynamic Dual-Modality Therapy System via Chitosan Hybrid Nanospheres. *Biomaterials* **2013**, *34*, 8314−8322.

(43) Chen, Q.; Yu, H. J.; Wang, L.; Abdin, Z.-u.; Yang, X. P.; Wang, J. H.; Zhou, W. D.; Zhang, H. T.; Chen, X. Synthesis and Character-ization of Amylose Grafted Poly(acrylic acid) and Its Application in Ammonia Adsorption. *Carbohydr. Polym.* **2016**, *153*, 429−434.

(44) Bardajee, G. R.; Hooshyar, Z. Interaction of a Novel Starch-Capped CdS Quantum Dots with Human Serum Albumin and Bovine Serum Albumin. *Starch-Stärke* **2016**, *68*, 329−338.

(45) Amaral, I. F.; Granja, P. L.; Barbosa, M. A. Chemical Modification of Chitosan by Phosphorylation: an XPS, FT-IR and SEM Study. *J. Biomater. Sci., Polym. Ed.* **2005**, *16*, 1575−1593.

(46) Matheson, I. B. C.; Lee, J.; Yamanashi, B. S.; Wolbarsht, M. L. Measurement of the Absolute Rate Constants for Singlet Molecular Oxygen (1.DELTA.g) Reaction with 1,3-Diphenylisobenzofuran and Physical Quenching by Ground State Molecular Oxygen. *J. Am. Chem. Soc.* **1974**, *96*, 3343−3348.

(47) Li, G. L.; Guo, C. S.; Yan, M.; Liu, S. Q. Cs$_x$WO$_3$ Nanorods: Realization of Full-Spectrum-Responsive Photocatalytic Activities from UV, Visible to Near-Infrared Region. *Appl. Catal., B* **2016**, *183*, 142−148.

(48) Kuo, W. S.; Chang, Y. T.; Cho, K. C.; Chiu, K. C.; Lien, C. H.; Yeh, C. S.; Chen, S. J. Gold Nanomaterials Conjugated with Indocyanine Green for Dual-Modality Photodynamic and Photo-thermal Therapy. *Biomaterials* **2012**, *33*, 3270−3278.

(49) Shibu, E. S.; Hamada, M.; Murase, N.; Biju, V. Nanomaterials Formulations for Photothermal and Photodynamic Therapy of Cancer. *J. Photochem. Photobiol., C* **2013**, *15*, 53.